IEEE Access
Multidisciplinary | Rapid Review | Open Access Journal

Received May 24, 2021, accepted June 3, 2021, date of publication June 8, 2021, date of current version June 21, 2021.

Digital Object Identifier 10.1109/ACCESS.2021.3087499

Improved Analytical Algorithm for Magnetic Field of End Windings in 300Mvar Synchronous Condenser

ERHANG ZHU, YANPING LIANG, XIAO HAN, XU BIAN, AND CHENGUANG WANG
College of Electrical and Electronic Engineering, Harbin University of Science and Technology, Harbin 150080, China

Corresponding author: Yanping Liang (liangyanping2010@126.com)

This work was supported in part by the Natural Science Foundation of Heilongjiang Province of China under Grant ZD2019E008, and in part by the University Nursing Program for Young Scholars with Creative Talents in Heilongjiang Province under Grant UNPYSCT-2018210.

ABSTRACT The magnetic field of end windings affects the leakage reactance of end windings and the eddy current losses of end structures in the large electrical machine. With the rising of single-machine capacity, such effect becomes more obvious. However, due to the complexity of end structures of large electrical machine, it will cause difficulty in meshing and long calculation time to calculate the magnetic field of end windings by using 3-D finite element method (FEM). In order to calculate the magnetic field of end windings quickly and accurately, an improved analytical algorithm (IAA) is proposed based on the mirror image principle, which takes into account the influence of stator back core and air-gap on the magnetic field of end windings by adding the fictitious boundary current and air-gap current, respectively. Taking a 300Mvar synchronous condenser (SC) as an example, the boundary current, air-gap current and magnetic field of end windings are calculated. Then, the influence of stator back core and stator involute segment current on the magnetic field of end windings are analyzed, which provides a theoretical support for the design and optimization of SC. To validate the accuracy of IAA, the calculation result is compared with 3-D FEM.

INDEX TERMS Synchronous condenser, magnetic field, analytical algorithm, mirror image, stator back core.

I. INTRODUCTION

With the strong instantaneous reactive power support and short-time overload capability, the SC has been used as an indispensable reactive power compensation device for today's power grid [1], [2]. Fig.1 shows the new 300Mvar SC, which works alternately under multi-operating conditions. When the SC works under deep leading phase operation, sharply increased stator current will threaten the stable operation of SC and power grid seriously. Therefore, the design of SC is facing new challenges. In view of the mentioned characteristics of SC, a fast and accurate method for calculating the leakage reactance of end windings and the eddy current losses of end structures of SC are of great necessity.

3-D FEM and analytical method are two main methods for calculating the above problems. Based on 3-D transient FEM, the magnetic field and eddy current losses in the end region of large electrical machine were calculated in [3], [4], and the temperature distribution in the end region of the water–hydrogen cooled turbine generator was calculated in [5]–[8]. The 3-D electromagnetic force distribution in end region of turbine generator was calculated by a 3-D FEM

FIGURE 1. New 300Mvar SC.

The associate editor coordinating the review of this manuscript and approving it for publication was Paolo Giangrande.

in [9], [10]. Although 3-D FEM is with high calculation precision, there are still many shortcomings in the construction of 3-D model, calculation time and meshing. A complete set of analytical method for calculating the magnetic field and eddy current losses in the end structures of turbine generator was first proposed by P. Hammond in [11]–[15]. The formula for end-winding current distribution replaced by equivalent current sheets of the sinusoidal type was derived in [16], [17]. On this basis, the analytical method was employed to calculate the eddy current losses in the clamping ring of turbine generator in [18]. Based on the mirror image principle, the leakage inductance of end windings of motor was calculated by a 3-D analytic method in [19]–[22], which assume that the permeability of end core was infinite. Compared with the 3-D FEM, the analytical method requires only a short calculation time for calculating the magnetic field of end windings of large electrical machine. However, due to the low calculation accuracy, the analytical method is still rarely used to calculate the magnetic field of end windings of large electrical machine.

The magnetic field of end winding is very important in the simulation calculation of large electrical machine. It is the basis for calculating the eddy current losses, which can provide a theoretical support for the estimation of stray loss. It is also useful in calculating the leakage reactance and electromagnetic force of end windings. In [16], the magnetic field of end windings in turbine generator was calculated, and it was verified that the eddy current in clamping ring has little effect on its surface magnetic field. In [17], the eddy current losses in clamping ring of turbine generator were calculated by the magnetic field of end windings and the eddy current feedback coefficient. In [12], the magnetic field of end windings is calculated and the influence factors of stray loss are analyzed in rotating electrical machine. As the capacity of a single machine increases, it is necessary to analyze the magnetic field of end windings.

In this paper, an IAA for calculating the magnetic field of end windings in large electrical machine is proposed, which is based on the mirror image principle. This algorithm takes into account the influence of stator back core and air-gap on the magnetic of end windings by adding the fictitious boundary current and air-gap current, respectively. The boundary current, air-gap current and the magnetic field of end windings in 300Mvar SC are calculated. Then, the influence of stator back core and the stator involute segment current on the end magnetic field is analyzed in detail. In order to verify the correctness of the proposed analytical algorithm, the calculation results are compared with that of 3-D FEM.

II. ANALYSIS METHOD OF THE MAGNETIC FIELD

A. BASIC ASSUMPTION

In order to verify the accuracy of the IAA more easily, the following some assumptions are necessary:

1) The stator winding is replaced by serial filaments whose path is located in the center of stator winding. The section of stator winding is small. This approximation is good results at points relatively far away from the stator windings, which are what we need.
2) The permeability of stator and rotor core is infinite. With the rising of stator and rotor core saturation, the permeability of stator and rotor core gradually decreases. However, the permeability of stator and rotor core is still much greater than the vacuum permeability when the SC works under loss of field operation. According to the mirror image principle, the mirror current can be approximately equal to the source current. Such assumption can simplify the calculation of the magnetic field of end windings.
3) The influences of slots and end structures are neglected. The end structures are non-magnetic, and the eddy currents in end structures have little effect on its surface magnetic field [17]. From a field point of view, slots have little effect on the magnetic field of end windings.
4) The SC works under loss of field operation.
5) The stator current is varying sinusoidally over time.

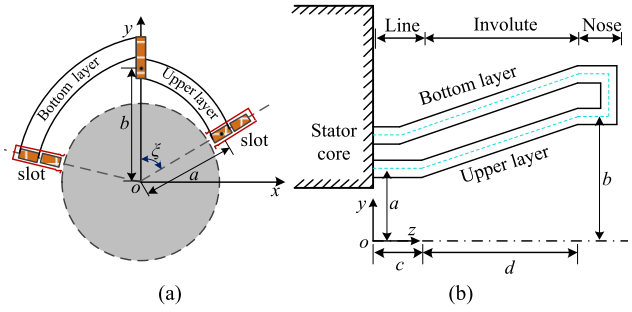

FIGURE 2. Schematic diagram of stator end winding. (a) *xy* plane, (b) *yz* plane.

B. STATOR WINDING

The coordinate of stator end winding involute is difficult to obtain, the stator end winding, therefore, was replaced by one or more cylindrical surfaces in the previous calculation of end magnetic field. It is analyzed as a focus in this section. The schematic diagram of stator end winding is shown in Fig. 2. The involute equations of upper layer stator end winding are as follows:

$$\begin{cases} x(t) = (a + (b - a)t) \cdot \cos(\xi t) \\ y(t) = (a + (b - a)t) \cdot \sin(\xi t) \\ z(t) = c + dt \end{cases} \tag{1}$$

where a is the distance from the line segment to the z axis, b is the distance from the nose segment to the z axis, c is the distance of the line segment, d is the projection distance of the involute segment on the z axis, ξ is the rotation angle of the starting point and ending point of the involute segment in the xy plane, and $t \in [0, 1]$. In the analytical calculation, 3-D stator end windings are modeled by serial connected filaments, which are shown in Fig 3.

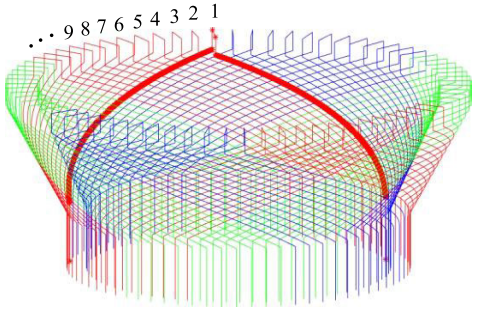

FIGURE 3. 3-D stator end windings modeled by serial connected filaments.

C. BOUNDARY CURRENT

Before introducing the IAA, it is helpful to consider a simpler model. Fig. 4 shows the magnetic field distribution of a current-carrying coil near semi-infinite iron core. In Fig. 4, μ_0 is the permeability of vacuum and μ_{Fe} is the permeability of core. Point P is on boundary surface S_1, α is the angle of magnetic lines passing through point P. The magnetic lines pass almost perpendicularly through the boundary surfaces S_1 and S_2. The magnetic field distribution obtained by calculating such a structure based on the mirror image principle is shown in Fig. 5. The boundary surface S_2 is taken as the mirror surface, and the mirror current I' is equal to original current I. Comparing Fig. 4 and Fig. 5, the angles of magnetic lines passing through the boundary surface S_2 are the same substantially, but the closed path of magnetic lines through the boundary surface S_1 is prolonged in Fig. 5. According to the Ampere' law, the magnetic flux density calculated by the mirror image principle is smaller than the actual value.

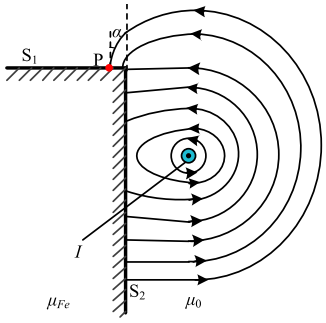

FIGURE 4. Magnetic field distribution of a carrying-current coil near semi-infinite iron core.

In order to reduce the error caused by the boundary surface S_1, an improved mirror image method is proposed on the basis of the mirror principle. A set of fictitious boundary coils whose current-carrying direction is opposite to the original current's is added in the periphery of boundary surface S_1, so that the angle of magnetic lines passing through boundary surface S_1 is perpendicular as much as possible. The magnetic field distribution calculated by the improved mirror image method is shown in Fig. 6, where b_0 is the distance from the

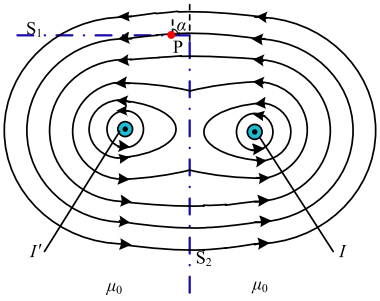

FIGURE 5. Magnetic field distribution of a current-carrying coil near semi-infinite iron core calculated by the mirror image principle.

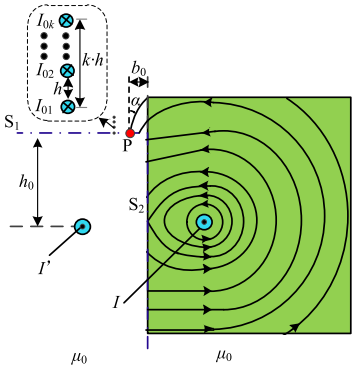

FIGURE 6. Magnetic field distribution of a current-carrying coil near semi-infinite iron core calculated by the improved mirror method.

point P to the boundary surface S_2, h is the distance between two adjacent boundary coils, $k \cdot h$ is the distance from the kth fictitious boundary coil to the boundary surface S_1, h_0 is the distance from the fictitious mirror image coil to the boundary surface S_1, and I_{0k} is boundary current of the kth layer. The calculation result is more accurate when $k \cdot h \approx 0.2h_0$, $b_0 \approx 0.01h_0$.

D. EQUIVALENT AIR-GAP CURRENT

The air-gap magnetomotive force has a great effect on magnetic field of end windings in large electrical machine. The electrical machine model with a full-pitched coil is shown in Fig 7(a). In Fig 7(a), g is the air-gap length and $c_1c_2c_3c_4c_5c_6$ is the magnetic line induced by the coil. The magnetic field strength is:

$$\begin{cases} H_{c_1c_2} = H_{c_3c_4} = H_{c_5c_6} = H_{c_6c_1} = 0 \\ H_{c_2c_3} = H_{c_4c_5} = I_{\mathrm{ui}}/2g. \end{cases} \tag{2}$$

The air-gap effect can be considered by filling the air-gap and slot with ferromagnetic material and adding a fictitious coil carrying equivalent air-gap current in the air-gap center, as shown in Fig 7(b). In Fig 7(b), R_g is the radius of fictitious equivalent air-gap coil. I_{ui} and I_{di} are the current of upper layer winding and bottom layer winding in the ith slot. The value of equivalent air-gap current on both sides of the slot is the same, but the direction is opposite.

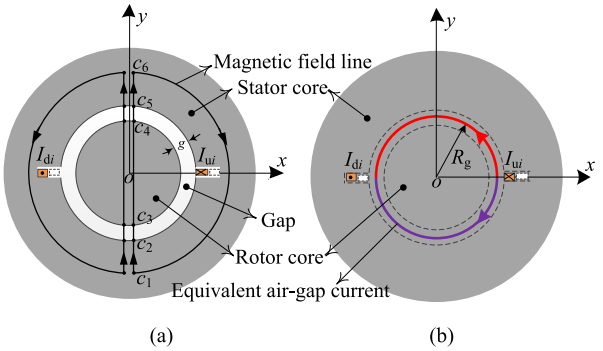

FIGURE 7. Electrical machine model. (a) Full-pitched coil. (b) Equivalent air-gap current.

III. IMPROVED ANALYTICAL ALGORITHM FOR THE MAGNETIC FIELD OF END WINDINGS IN 300Mvar SC

2-pole 300Mvar SC is taken as an example. The main parameters are shown in Table 1.

TABLE 1. Main parameters.

Symbol	Value
Rated capacity	300 Mvar
Rated voltage	20 kV
Rated excitation current	2325 A
Rated frequency	50 Hz
Number of stator slots	72
Air-gap length	71 mm
Radius of rotor core	635 mm
Outer radius of stator core	1475 mm
Number of pole pairs	2
Nominal speed	3000 r/min
Stack length	5900 mm
Phase current under loss of field condition	5248 A

A. CALCULATION OF BOUNDARY CURRENT

The schematic diagram of IAA at the end of SC in yz plane is shown in Fig. 8. In Fig. 8, q_2q_3 and q_4q_5 are the involute segments of upper layer winding and the bottom layer winding, respectively. q_1q_8 and q_6q_7 are mirror images of q_2q_3 and q_4q_5. I'_{uj} and I'_{dj} are the mirror images of upper layer current I_{uj} and bottom layer current I_{dj}, respectively. The fictitious coils carrying boundary current are added to the periphery of stator core. The region V contains the positions where all end structures of SC are located. The schematic diagram of IAA at the end of SC in xy plane is shown in Fig. 9, where $I_{0k,n}$ is the boundary current of the nth segment of the kth layer. The boundary current of each layer is equally divided into n segments.

According to Biot-savart law, the equation for calculating magnetic flux density is expressed as follows:

$$(B_x, B_y, B_z) = \frac{\mu_0 I}{4\pi} \int_l \frac{(dl_x, dl_y, dl_z) \times (\rho_x, \rho_y, \rho_z)}{|\boldsymbol{\rho}|^3} \quad (3)$$

where B_x, B_y and B_z are the magnetic flux densities in x, y and z directions, respectively. $|\boldsymbol{\rho}|$ is the distance between

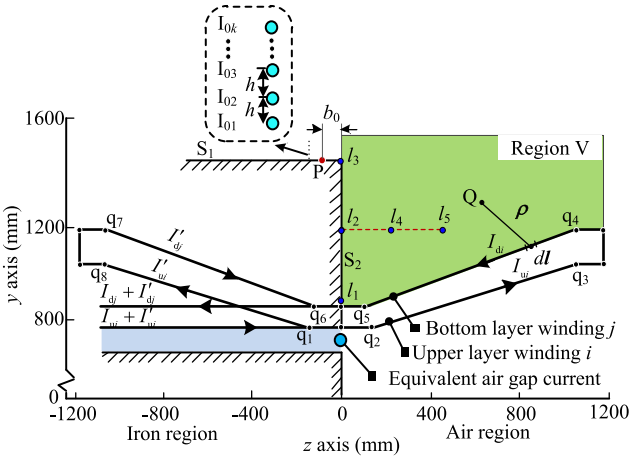

FIGURE 8. Schematic diagram of IAA at the end of SC in *yz* plane.

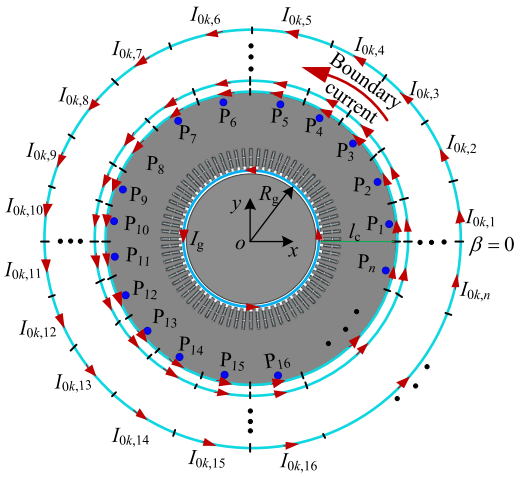

FIGURE 9. Schematic diagram of IAA at the end of SC in *xy* plane.

infinitesimal $d\boldsymbol{l}$ and any point Q in region A. dl_x, dl_y and dl_z are the projections of infinitesimal $d\boldsymbol{l}$ in x, y *and* z directions, respectively. ρ_x, ρ_y and ρ_z are the projections of $\boldsymbol{\rho}$ in x, y *and* z directions, respectively.

In the IAA, the integral path is considered to be composed of discrete points. The integral is obtained on each small discrete path, and the magnetic field induced by a conductor is obtained by summing the magnetic field induced by each small discrete path on the conductor. The expression for solving the magnetic flux density by the discrete integration method is:

$$(B_x, B_y, B_z) = \frac{\mu_0 I}{4\pi} \sum \frac{(\Delta l_x, \Delta l_y, \Delta l_z) \times (\rho_x, \rho_y, \rho_z)}{|\boldsymbol{\rho}|^3} \quad (4)$$

where Δl_x, Δl_y and Δl_z are the projections of infinitesimal Δl in x, y *and* z directions. The space angle α at point P_n can

be expressed as follows:

$$\begin{cases} \dfrac{\sum_{i=1}^{m}\left(B_{\mathrm{u}zi}^{(n)}+B_{\mathrm{d}zi}^{(n)}\right)+\sum_{k=1}^{k_1}\sum_{n=1}^{n_1}B_{0zk,n}^{(n)}}{\sqrt{\left(\sum_{i=1}^{m}\left(B_{\mathrm{u}xi}^{(n)}+B_{\mathrm{d}xi}^{(n)}\right)+\sum_{k=1}^{k_1}\sum_{n=1}^{n_1}B_{0xk,n}^{(n)}\right)^2+\left(\sum_{i=1}^{m}\left(B_{\mathrm{u}yi}^{(n)}+B_{\mathrm{d}yi}^{(n)}\right)+\sum_{k=1}^{k_1}\sum_{n=1}^{n_1}B_{0yk,n}^{(n)}\right)^2}} = \tan(\alpha), \\ \qquad \sum_{i=1}^{m}\left(B_{\mathrm{u}zi}^{(n)}+B_{\mathrm{d}zi}^{(n)}\right)\geq 0 \\ \dfrac{\sum_{i=1}^{m}\left(B_{\mathrm{u}zi}^{(n)}+B_{\mathrm{d}zi}^{(n)}\right)+\sum_{k=1}^{k_1}\sum_{n=1}^{n_1}B_{0zk,n}^{(n)}}{\sqrt{\left(\sum_{i=1}^{m}\left(B_{\mathrm{u}xi}^{(n)}+B_{\mathrm{d}xi}^{(n)}\right)+\sum_{k=1}^{k_1}\sum_{n=1}^{n_1}B_{0xk,n}^{(n)}\right)^2+\left(\sum_{i=1}^{m}\left(B_{\mathrm{u}yi}^{(n)}+B_{\mathrm{d}yi}^{(n)}\right)+\sum_{k=1}^{k_1}\sum_{n=1}^{n_1}B_{0yk,n}^{(n)}\right)^2}} = -\tan(\alpha), \\ \qquad \sum_{i=1}^{m}\left(B_{\mathrm{u}zi}^{(n)}+B_{\mathrm{d}zi}^{(n)}\right)<0 \end{cases} \tag{5}$$

where $B_{\mathrm{u}xi}^{(n)}$, $B_{\mathrm{u}yi}^{(n)}$ and $B_{\mathrm{u}zi}^{(n)}$ are the magnetic flux densities induced by the ith upper layer winding current and its mirror image at point P_n, $B_{\mathrm{d}xi}^{(n)}$, $B_{\mathrm{d}yi}^{(n)}$, $B_{\mathrm{d}zi}^{(n)}$ are the magnetic flux densities induced by the ith bottom layer winding and its mirror image at point P_n, $B_{0xk,n}^{(n)}$, $B_{0yk,n}^{(n)}$ and $B_{0zk,n}^{(n)}$ are the magnetic flux densities induced by the boundary current of the nth segment of the kth layer at point P_n. m is the number of stator slots. k_1 and n_1 is the number of layers and segments of the boundary current. In order to simplify the calculation, it is assumed that the boundary current of the nth segment of each layer is equal. Taking $k = 7$ and $\alpha = \pi/180$ rad, the boundary current can be calculated by (4) and (5).

B. CALCULATION OF EQUIVALENT AIR-GAP CURRENT

The equivalent air-gap current can be determined according to the stator current and its spatial position. Assuming the equivalent air-gap current is positive in the counterclockwise direction, the equation of equivalent air-gap current derived from the winding current in the ith stator slot in the SC is:

$$I_{gi}(\beta)=\begin{cases} \dfrac{I_{ui}+I_{di}}{2}, & \dfrac{2\pi\times i}{m}\leq\beta<\dfrac{2\pi\times i}{m}+\pi \\ -\dfrac{I_{ui}+I_{di}}{2}, & 0\leq\beta<\dfrac{2\pi\times i}{m}, \\ & \dfrac{2\pi\times i}{m}+\pi\leq\beta<2\pi \end{cases} \tag{6}$$

where $1 \leq i \leq m/2$. The initial position of rotation angle β is shown in Fig. 9. I_{gi} is the equivalent air-gap current derived from the winding current in the ith slot. The equivalent air-gap current I_g of SC can be obtained by summing I_{gi}:

$$I_g(\beta)=\sum_{i=1}^{m/2}I_{gi}(\beta). \tag{7}$$

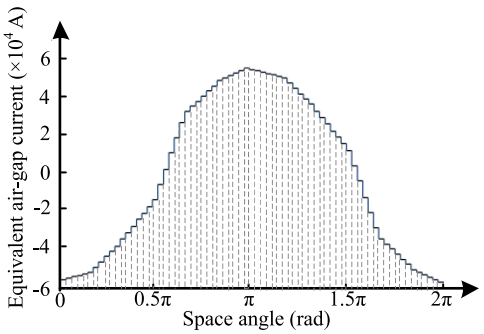

FIGURE 10. Equivalent air-gap current at a certain time.

The fictitious equivalent air-gap coil and its mirror image are in the same spatial position, and the mirror of equivalent air-gap current is as follows:

$$I_{\mathrm{gmir}}(\beta)=I_{\mathrm{g}}(\beta) \tag{8}$$

The equivalent air-gap current at a certain time under loss of field operation is shown in Fig. 10, which changes stepwise.

C. CALCULATION OF MAGNETIC FLUX DENSITY OF END WINDINGS

After the boundary current and the equivalent air-gap current are calculated, the magnetic field distribution of end windings in the SC can be easily obtained by using Biot-savart law and the principle of superposition. The calculation equation of end magnetic field is as follows:

$$\begin{cases} B_{\mathrm{e}x}=B_{\mathrm{w}x}+B_{\mathrm{g}x}+B_{\mathrm{gmir}x}+B_{\mathrm{b}x} \\ B_{\mathrm{e}y}=B_{\mathrm{w}y}+B_{\mathrm{g}y}+B_{\mathrm{gmir}y}+B_{\mathrm{b}y} \\ B_{\mathrm{e}z}=B_{\mathrm{w}z}+B_{\mathrm{g}z}+B_{\mathrm{gmir}z}+B_{\mathrm{b}z}. \end{cases} \tag{9}$$

where $B_{\mathrm{e}x}$, $B_{\mathrm{e}y}$ and $B_{\mathrm{e}z}$ are the magnetic flux densities of end wingdings. $B_{\mathrm{w}x}$, $B_{\mathrm{w}y}$ and $B_{\mathrm{w}z}$ are the magnetic flux densities induced by the stator current and its mirror image. $B_{\mathrm{g}x}$, $B_{\mathrm{g}y}$ and $B_{\mathrm{g}z}$ are the magnetic flux densities induced by the equivalent air-gap current. $B_{\mathrm{gmir}x}$, $B_{\mathrm{gmir}y}$ and $B_{\mathrm{gmir}z}$ are the magnetic flux densities induced by the mirror of the equivalent air-gap current. $B_{\mathrm{b}x}$, $B_{\mathrm{b}y}$ and $B_{\mathrm{b}z}$ are the magnetic flux densities induced by the boundary current.

IV. FINITE ELEMENT VERIFICATION AND ANALYSIS OF MAGNETIC FIELD OF END WINDINGS

A. FINITE ELEMENT VERIFICATION

Convert the x, y and z direction components of the magnetic flux density of end windings in the Cartesian coordinate system to the cylindrical coordinate system. The conversion equation is as follows:

$$\begin{cases} B_{\mathrm{e}r}=B_{\mathrm{e}x}\cos(\beta)+B_{\mathrm{e}y}\sin(\beta) \\ B_{\mathrm{e}\theta}=-B_{\mathrm{e}x}\sin(\beta)+B_{\mathrm{e}y}\cos(\beta) \\ B_{\mathrm{e}z}=B_{\mathrm{e}z} \end{cases} \tag{10}$$

where B_{er}, $B_{e\theta}$ and B_{ez} are the magnetic flux densities of end windings in the cylindrical coordinate system.

In 3-D FEM, the finite-element calculation model of end region in 300Mvar SC is shown in Fig. 11. The 3-D solution mesh of end region is shown in Fig. 12(a). The first-order tetrahedral elements are used to solve the end region. The solution mesh of local region of the stator winding is shown in Fig. 12(b). In Fig. 12(b), S_a, S_b, S_c are the outer surfaces of end solved region. The total number of meshes divided in the end region of SC is 2819844, the Newton iteration accuracy is 0.1%, and the conjugate gradient iteration accuracy is 0.0001%.

The magnetic flux density of end windings on space curves in Table 2 calculated by the IAA and 3-D FEM are shown in Fig. 13. In Table 2, $r = 920$ mm is the radial distance from the bottom of stator slot to the origin of coordinates, and $r = 1475$ mm is the outer radius of the stator core.

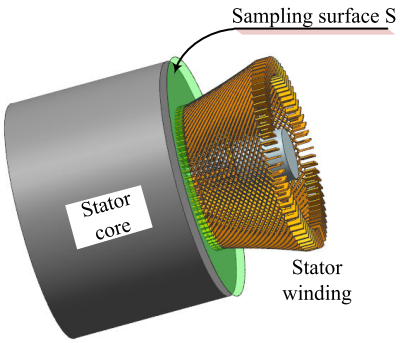

FIGURE 11. Finite-element calculation model of end region.

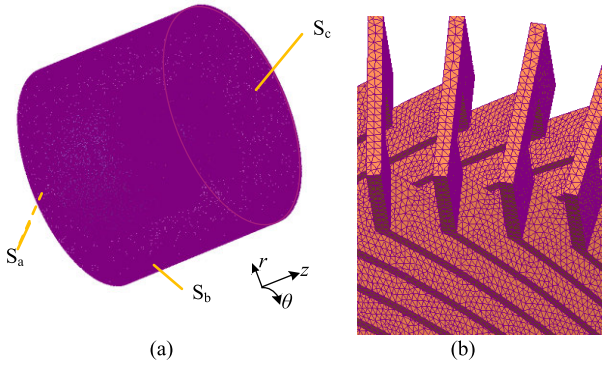

FIGURE 12. 3-D solution mesh of end region. (a) Solved region, (b) Local region of stator winding.

In Fig. 13, the results calculated by the IAA are very close to those calculated by the 3-D FEM. The radial and circumferential components of magnetic flux density of end windings from curve l_1 to curve l_5 are shown in Fig. 13(a) and 13(b), respectively. Comparing with curves l_1, l_2 and l_3, the radial and circumferential components of magnetic flux density decrease gradually with the increase of r. Comparing with curves l_2, l_4 and l_5, the radial and circumferential components of magnetic flux density increase gradually with the increase of z, because the spatial curve gradually approaches the involute segment. The radial and circumferential components of magnetic flux density of end windings are mainly induced by the involute segment current. Fig. 13(c) shows the axial component of magnetic flux density of end windings from curve l_1 to curve l_5. As r or z increases, the axial component of magnetic flux density of end windings decreases gradually. The axial component of magnetic flux density of end windings is very large near the stator slot.

TABLE 2. Space curves in the end region of SC.

Curve	r (mm)	z (mm)
l_1	920	0
l_2	1200	0
l_3	1475	0
l_4	1200	200
l_5	1200	400

The total calculation time of 3-D FEM is over 400 minutes. The maximum usage rate of 56-core CPU is 30% and the maximum memory usage is 31 GB. The calculation time of the IAA is about 15 minutes, which is more time-saving and convenient than the FEM.

B. ANALYSIS OF MAGNETIC FLUX DENSITY OF END WINDINGS

The radial, circumferential and axial components of magnetic flux density of end windings in the sampling surface S shown in Fig. 11 are shown in Figs. 14(a), 14(b), and 14(c). The inner radius of sampling surface S is 920mm, the outer radius is 1475mm, and the distance from the stator end surface is 50mm. The magnetic flux density of end windings is distributed sinusoidally, and the axial component of magnetic flux density of end windings is very larger than its radial and circumferential components. The circumferential component of magnetic flux density of end windings is the smallest. When z is constant, the three components of magnetic flux density of end windings gradually decrease with the increase of r, which is caused by the sampling curve gradually moving away from the air-gap and stator winding.

The influence of stator back core on the magnetic field of end windings is neglected in the traditional analysis algorithm (TAA). Take a straight line l_c at $\beta = 0$ rad on the surface of stator core as the sampling line, which show in Fig. 9. The magnetic flux densities on the l_c calculated by the TAA, IAA and FEM are compared, as shown in Fig. 15. In Fig. 15, when $r < 1325$ mm, the calculation results of the three methods are basically consistent. When $r > 1325$ mm, the magnetic flux density calculated by the TAA have a large calculation error. However, the magnetic flux density calculated by the IAA is very close to that calculated by the FEM in this region. The end structures are relatively large in large electrical machine. According to the calculation principle of eddy current losses,

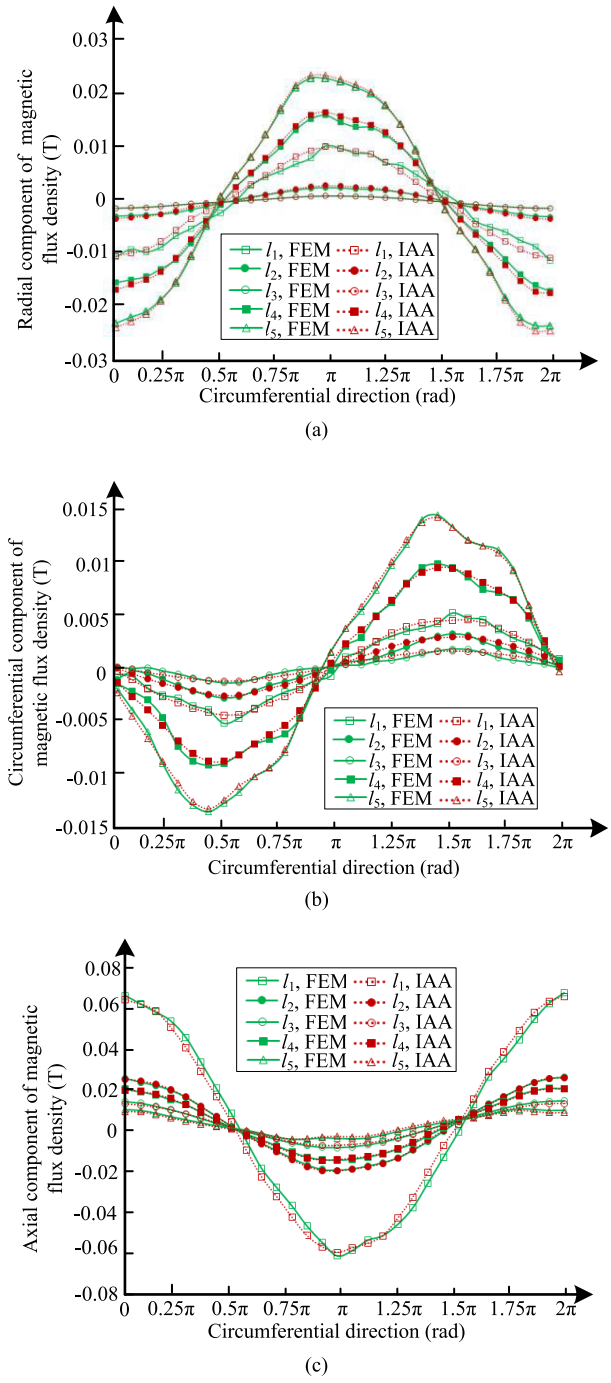

FIGURE 13. Magnetic flux density of end windings calculated by IAA and 3-D FEM. (a) Radial component, (b) Circumferential component, (c) Axial component.

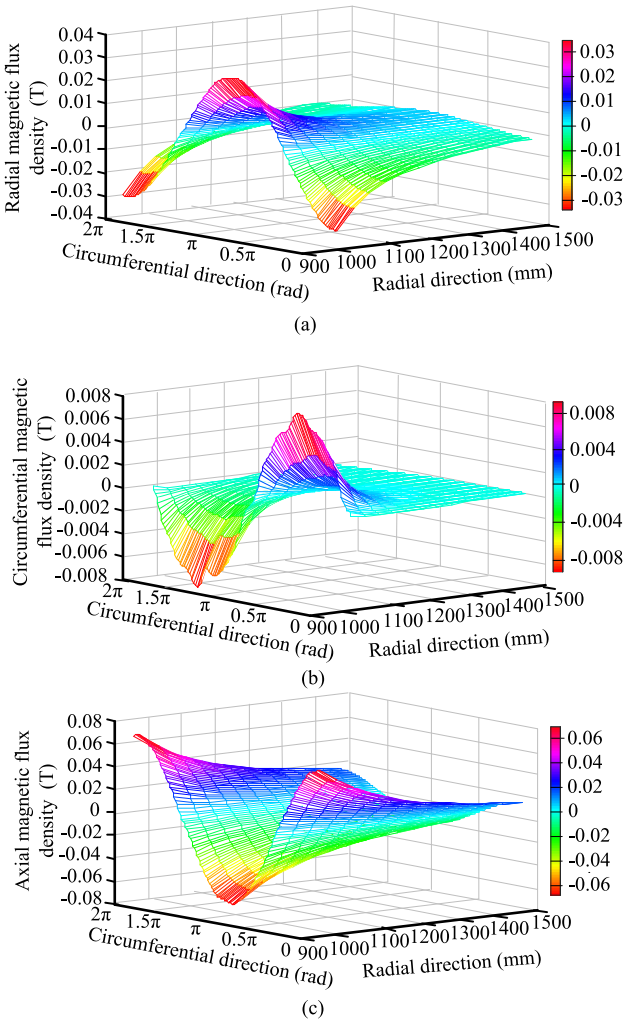

FIGURE 14. The magnetic flux density of end windings on the sampling surface S. (a) Radial component, (b) Circumferential component, (c) Axial component.

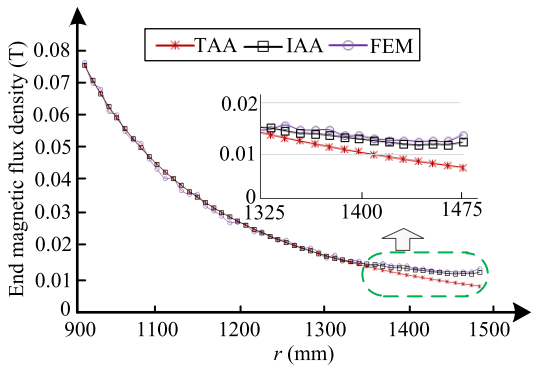

FIGURE 15. The magnetic flux density of l_c.

if the magnetic flux density calculated by the IAA is used to calculate the eddy current losses in the structure, the calculation accuracy will be significantly improved.

The axial component of magnetic flux density of end windings is the main influencing factor for the eddy current losses in the end structure of large electrical machine. In order to better analyze the influence of the involute segment current on the axial component of magnetic flux density of end windings, it is divided into two parts. The first part (called A_1) is the axial component of magnetic flux density induced by the involute segment current and its mirror image. The second part (called A_2) is the axial component of magnetic flux density induced by the air-gap current and its mirror image and boundary current. Assume that A (the vector sum

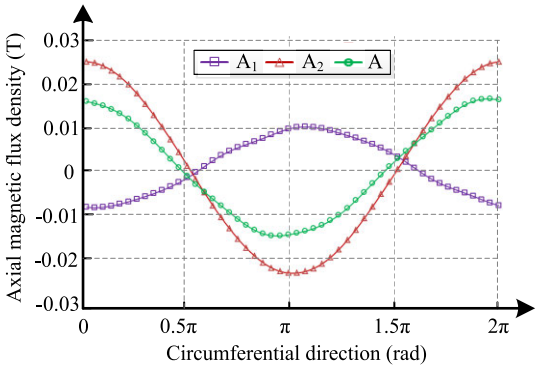

FIGURE 16. The distribution of A_1, A_2 and A on the curve l_a.

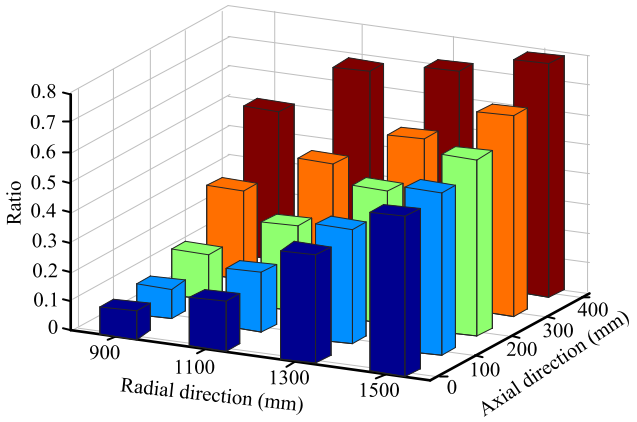

FIGURE 17. The ratio of peak values of A_1 and A_2 on circular curves.

of A_1 and A_2) is the axial component of magnetic flux density in the SC. The distribution of A_1, A_2 and A on the curve l_a ($r = 1200$, $z = 50$) are shown in Fig.16. It is almost at any point on the curve l_a that the directions of A_1 and A_2 are opposite, and the absolute value of A_2 is greater than A_1. A_1 has a demagnetization effect on the axial component of magnetic flux density. The ratio of peak values of A_1 and A_2 on different circular curves is shown in Fig. 17. As r or z increases, the influence of A_1 on the magnetic flux density of end windings increases.

V. CONCLUSION

In this paper, an IAA is proposed for calculating the magnetic field of end windings in the large electrical machine, which is based on mirror image principle. The influence of stator back core on the magnetic field of end windings is considered by adding a set of fictitious coils carrying boundary currents on the periphery of stator core, which reduces the calculation error of magnetic flux density of end windings around the outer diameter of stator core.

The magnetic field of end windings of 300Mvar SC is calculated and analyzed, which is a key step to calculate the eddy current losses of end structures. When the sampling curve is close to the ferromagnetic surface, the axial component of magnetic flux density of end windings is much larger than the radial and circumferential components of magnetic flux density of end windings. When z is constant, the three components of magnetic flux density of end windings decrease with the increase of r. When r is constant, the farther the sampling curve is from the ferromagnetic surface, the larger the radial and circumferential components of magnetic flux density of end windings are, at the same time the smaller the axial component of magnetic flux density of end windings is. A_1 has a demagnetization effect on the axial component of magnetic flux density of end windings. As r or z increases, the effort of A_1 on the end magnetic flux density of end windings increases gradually.

The presented analytical algorithm is suitable for calculating the magnetic field of end windings of all large electrical machines, and it is verified by the 3-D FEM. Moreover, the IAA has a shorter calculation time, which can provide a good theoretical support for optimization design of large electrical machines, and is more suitable for engineering applications.

REFERENCES

[1] J. Jia, G. Yang, A. H. Nielsen, and P. Rønne-Hansen, "Impact of VSC control strategies and incorporation of synchronous condensers on distance protection under unbalanced faults," *IEEE Trans. Ind. Electron.*, vol. 66, no. 2, pp. 1108–1118, Feb. 2019.

[2] A. Aamir, L. Qiao, C. Guo, A. U. Rehman, and Z. Yang, "Impact of synchronous condenser on the dynamic behavior of LCC-based UHVDC system hierarchically connected to AC system," *CSEE J. Power Energy Syst.*, vol. 5, no. 2, pp. 190–198, Jun. 2019.

[3] Y. Liang, H. Yu, and X. Bian, "Finite-element calculation of 3-D transient electromagnetic field in end region and eddy-current loss decrease in stator end clamping plate of large hydrogenerator," *IEEE Trans. Ind. Electron.*, vol. 62, no. 12, pp. 7331–7338, Dec. 2015.

[4] Y. Liang, X. Bian, H. Yu, and C. Li, "Finite-element evaluation and eddy-current loss decrease in stator end metallic parts of a large double-canned induction motor," *IEEE Trans. Ind. Electron.*, vol. 62, no. 11, pp. 6779–6785, Nov. 2015.

[5] H. Jichao, W. Chao, W. Yang, S. Yutian, and Z. Ping, "Influence of extension length of rotor end windings on the three-dimensional electromagnetic field and temperature rise in the large turbine generator end zone with magnetic screen," *IEEE Access*, vol. 8, pp. 70703–70712, 2020.

[6] Z.-N. Fan, Z.-Y. Bian, K. Xiao, J.-C. Li, B. Yao, and X.-G. Gan, "The electromagnetic-fluid-temperature field analysis of loss and heat of self-cooling separate-phase enclosed bus of large generator," *IEEE Access*, vol. 9, pp. 11372–11377, 2021.

[7] W. Liu, W. Li, S. Luo, X. Huang, D. Li, Z. Li, and G. Xu, "Influence of a novel stator teeth internal ventilation structure on air-cooled turbo-generator parameters and stator temperature," *IEEE Access*, vol. 8, pp. 122422–122433, 2020.

[8] Q.-L. Hu, K. Xiao, Z.-T. Zhou, Z.-N. Fan, Y. Yang, Z.-Y. Bian, J.-C. Li, and B. Yao, "3D transient electromagnetic-temperature field analysis of the loss and heat of the damper bars of a large tubular hydro-generator during short circuit faults," *IEEE Access*, vol. 8, pp. 135963–135974, 2020.

[9] R. D. Stancheva and I. I. Iatcheva, "3-D electromagnetic force distribution in the end region of turbogenerator," *IEEE Trans. Magn.*, vol. 45, no. 3, pp. 1000–1003, Mar. 2009.

[10] Z. Chong, H. Song, and Y. Yongming, "Analysis of electromagnetic forces on involute part of end winding in a 1550 MW nuclear generator," in *Proc. IEEE 2nd Adv. Inf. Technol., Electron. Autom. Control Conf. (IAEAC)*, Chongqing, China, Mar. 2017, pp. 1–4.

[11] P. Hammond, "The calculation of the magnetic field of rotating machines. Part 1: The field of a tubular current," *Proc. IEE C, Monographs*, vol. 106, no. 10, pp. 158–164, Sep. 1959.

[12] D. S. Ashworth and P. Hammond, "The calculation of the magnetic field of rotating machines. Part 2: The field of turbo-generator end-windings," *Proc. IEE A, Power Eng.*, vol. 108, no. 42, pp. 527–538, Dec. 1961.

[13] P. Hammond, "The calculation of the magnetic field of rotating machines. Part 3: Eddy currents induced in a solid slab by a circular current loop," *Proc. IEE C, Monographs*, vol. 109, no. 16, pp. 508–515, Sep. 1962.
[14] R. L. Stoll and P. Hammond, "Calculation of the magnetic field of rotating machines. Part 4: Approximate determination of the field and the losses associated with eddy currents in conducting surfaces," *Proc. Inst. Electr. Eng.*, vol. 112, no. 11, pp. 2083–2094, Nov. 1965.
[15] R. L. Stoll and P. Hammond, "Calculation of the magnetic field of rotating machines. Part 5: Field in the end region of turbogenerators and the eddy-current loss in the end plates of stator cores," *Proc. Inst. Electr. Eng.*, vol. 113, no. 11, pp. 1793–1804, Nov. 1966.
[16] J. A. Tegopoulos, "Flux impinging on the end plate of turbine generators," *Trans. Amer. Inst. Electr. Eng. III, Power App. Syst.*, vol. 81, no. 3, pp. 700–706, Apr. 1962.
[17] J. A. Tegopoulos, "Current sheets equivalent to end-winding currents of turbine-generator stator and rotor," *Trans. Amer. Inst. Electr. Eng. III, Power App. Syst.*, vol. 81, no. 3, pp. 695–700, Apr. 1962.
[18] X. Shanchun, "An analytical calculation of the end plate losses in the turbine generator," (in Chinese), *Large Electr. Mach. Hydraulic*, no. 2, pp. 1–11, 1989.
[19] D. Ban, D. Zarko, and I. Mandic, "Turbogenerator end-winding leakage inductance calculation using a 3-D analytical approach based on the solution of Neumann integrals," *IEEE Trans. Energy Convers.*, vol. 20, no. 1, pp. 98–105, Mar. 2005.
[20] A. Tessarolo and F. Luise, "An analytical-numeric method for stator end-coil leakage inductance computation in multi-phase electric machines," in *Proc. IEEE Ind. Appl. Soc. Annu. Meeting*, Edmonton, AB, Canada, Oct. 2008, pp. 1–8.
[21] Y. Liang, X. Bian, H. Yu, L. Wu, and B. Wang, "Analytical algorithm for strand end leakage reactance of transposition bar in AC machine," *IEEE Trans. Energy Convers.*, vol. 30, no. 2, pp. 533–540, Jun. 2015.
[22] X. Bian and Y. Liang, "Analysis on eddy current losses in stator windings of large hydro-generator considering transposed structure based on analytical calculation method," *IEEE Access*, vol. 7, pp. 163948–163957, 2019.

ERHANG ZHU was born in Hebei, China, in 1991. He is currently pursuing the Ph.D. degree in electrical machines with the Harbin University of Science and Technology, Harbin.

His research interests include research on electromagnetic, operation analysis, and design of large electrical machines.

YANPING LIANG was born in Harbin, China, in 1963. She received the M.S. degree in electrical machine from the Harbin University of Science and Technology, Harbin, in 1988, and the Ph.D. degree in electrical machines from the Harbin Institute of Technology, Harbin, in 2005. She is currently a Professor with the Harbin University of Science and Technology. Her research interests include electrical machine electromagnetic theory and design, large generator electromechanical energy conversion, and electromagnetic field calculation. She is a Senior Member of the China Electrotechnical Society.

XIAO HAN was born in Hebei, China, in 1993. She is currently pursuing the Ph.D. degree in electrical machines with the Harbin University of Science and Technology, Harbin, China.

Her research interests include research on electromagnetic, operation analysis, and design of large electrical machines.

XU BIAN was born in Harbin, China, in 1988. She received the B.S., M.S., and Ph.D. degrees in electrical machine from the Harbin University of Science and Technology, Harbin, in 2010, 2013, and 2016, respectively.

She is currently an Associate Professor with the Harbin University of Science and Technology. Her research interests include electromagnetic, fluid and thermal analysis, and design on electrical machines.

CHENGUANG WANG was born in Xingtai, China, in 1984. He received the B.S. and M.S. degrees in signal and information processing, and the Ph.D. degree in electrical machines from the Harbin University of Science and Technology, Harbin, China, in 2005, 2008, and 2020, respectively.

He is currently a Lecturer with the Harbin University of Science and Technology. His research interests include electromagnetic measurement technology and stator windings fault diagnosis.